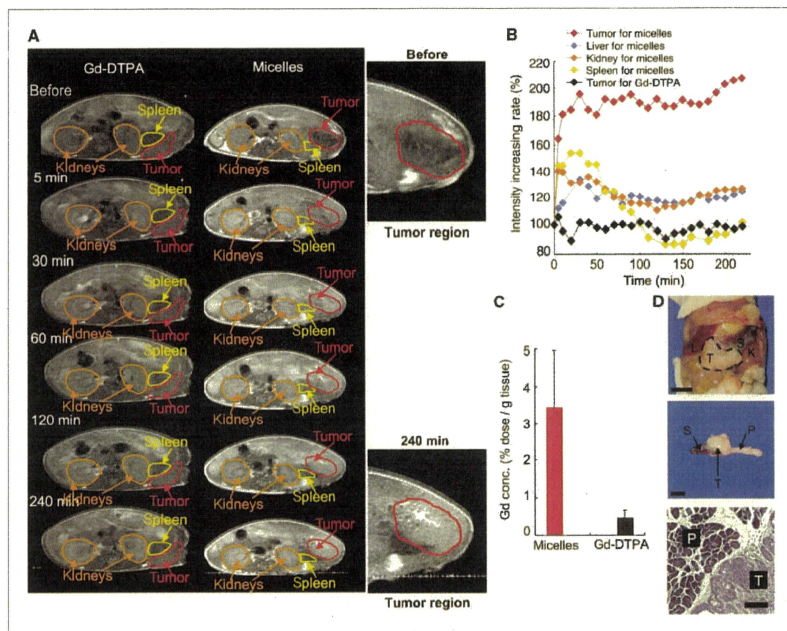Figure 3. In vivo behavior of Gd-DTPA/ DACHPt–loaded micelles. A, left, plasma clearance of Pt drugs after i.v. injection of oxaliplatin and Gd-DTPA/DACHPt–loaded micelles; right, plasma clearance of Gd complexes after i.v. injection of Gd-DTPA and Gd-DTPA/DACHPt–loaded micelles. B, left, accumulation of Pt drugs in the C-26 tumor after i.v. injection of oxaliplatin or Gd-DTPA/DACHPt–loaded micelles; right, accumulation of Gd complexes in C-26 tumors after i.v. injection of Gd-DTPA or Gd-DTPA/DACHPt–loaded micelles. C, left, in vivo MRI series of T_1-weighted transaxial slices of C-26 subcutaneous tumor after i.v. injection of Gd-DTPA/ DACHPt–loaded micelles or Gd-DTPA at 5 μmol/kg Gd-DTPA. Right, top, tumor-to-muscle intensity ratio for the micelles and Gd-DTPA at 5, 60, and 180 min; bottom, relative intensity enhancement in the tumor after i.v. injection of Gd-DTPA/DACHPt–loaded micelles or Gd-DTPA at 5 μmol/kg Gd-DTPA.
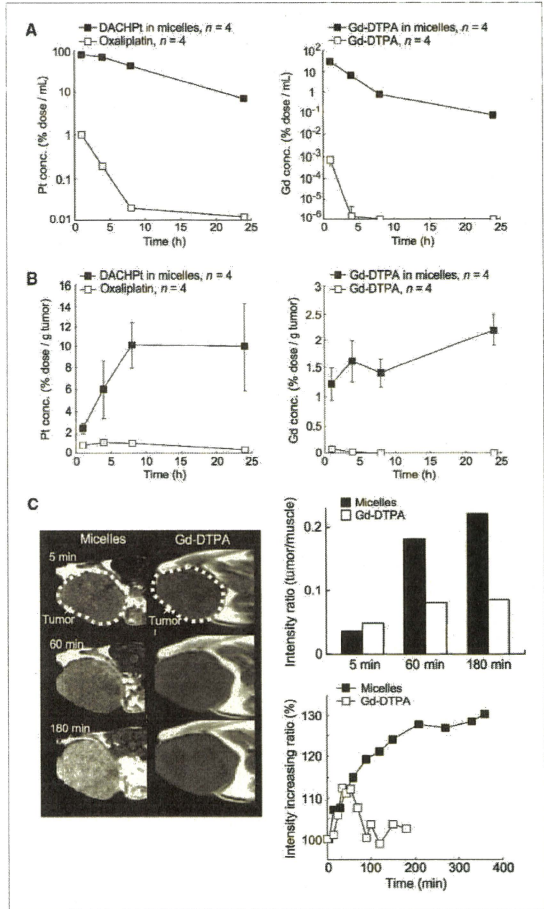
distribution of heme proteins. Accordingly, the PECAM-1–positive area from the immunofluorescence microscopy (Fig. 6A) showing the existence of endothelial cells is consistent with this Fe-rich area (Fig. 6B). The K-rich regions possibly correspond to pancreatic cancer cells because K is a cofactor required to obtain maximum activity of the pyruvate

kinase, an enzyme involved in glycolytic energy production, which has been observed in carcinoma tissue of the pancreas (31). The Gd as well as the Pt atoms located at those K-rich areas suggest the selective tumor accumulation of Gd-DTPA and DACHPt. Moreover, the colocalization of the Gd-DTPA and DACHPt confirms the high potential of Gd-DTPA/

Figure 4. *In vivo* behavior of Gd-DTPA/DACHPt–loaded micelles on an orthotopic pancreatic cancer (BxPC3). A, *in vivo* MRI series of T_1-weighted transaxial slices of mice after i.v. injection of Gd-DTPA/DACHPt–loaded micelles or Gd-DTPA at 5 μmol/kg. B, relative MRI intensity in each organ after i.v. injection of Gd-DTPA/DACHPt–loaded micelles at 5 μmol/kg Gd-DTPA or i.v. injection of Gd-DTPA at 5 μmol/kg. C, the Gd-DTPA/DACHPt–loaded micelles and Gd-DTPA accumulation in the BxPC3 tumor 4 h after i.v. administration ($n = 4$). D, top, macroscopic findings of orthotopic BxPC3-bearing BALB/c nude mice after MRI acquisition. Scale bar, 1 cm. Middle, the pancreatic tumor after excision with spleen and normal pancreas. Scale bar, 0.5 cm. Bottom, microscopic findings (H&E staining) of the pancreatic cancer (T) and normal pancreatic tissue (P). Scale bar, 100 μm.

DACHPt–loaded micelles to assess the distribution of the anticancer drug at the tumor site by MRI.

Discussion

Pancreatic cancer has one of the worst prognoses among cancers (32). The high malignancy of pancreatic adenocarcinoma prompts the destruction of the surrounding tissue, whereas the lack of serous membrane in healthy pancreas cannot prevent the dissemination of cancer cells. The microenvironment characteristics of the pancreatic adenocarcinoma, including hypovascularity and thick fibrosis, prevent the accumulation of drugs in the tumor tissue (33). Moreover, the anatomic position of the pancreas in the deep retroperitoneal space makes early detection difficult. Although computed tomography is widely used for the evaluation of pancreatic carcinoma in the clinical setting, MRI may better predict the therapeutic efficacy and the prognosis in patients with pancreatic cancer because of its superior contrast resolution of noncontour deforming lesions of the pancreas, small liver metastases, and peritoneal disseminations (34). Thus, the outstanding contrast enhancement achieved by Gd-DTPA/DACHPt–loaded micelles on this tumor model suggests the great potential of this modality for the clear detection of the lesions in the abdominal cavity and the facile recognition of the carcinomas of the pancreas as distinct from the surrounding internal organs by MRI.

The exceptionally bright contrast achieved by Gd-DTPA/DACHPt–loaded micelles can be attributed to the enhanced accumulation of the micelles at the tumor site and to the

augmentation of the relaxivity of the Gd-DTPA in the core of the micelles. The amount of Gd-DTPA delivered by the micelles in the orthotopic pancreatic tumor was >3% of the injected dose after 4 hours. Because the r_1 of Gd-DTPA in the micelles is 24 times higher than that of free Gd-DTPA, the resulting contrast enhancement probably mimics a much higher accumulation level. In this regard, it has been reported that the r_1 of Gd-based MRI contrast agents increases after binding with polymers or proteins due to the flexibility reduction per Gd molecule and the increase of the rotational correlation time (τ_R; ref. 35). Moreover, Livramento and colleagues (36) suggested that an Fe/Gd chelate, a metallostar Fe{Gd$_2$(bipyridine(diethylenetriaminetetraacetic acid)$_2$(H$_2$O)$_4$)$_3$}$^{4-}$ structure, showed a high relaxivity because the inner-sphere water molecules presented an exchange rate (τ_m) close to the optimal value in addition to the increasing τ_R. In our system, the formation of the Gd-DTPA/DACHPt–loaded micelles probably combined an increase of the τ_R and the optimization

of the τ_m in the hydrophobic environment at the micelle core, leading to the increase in relaxivity. Further studies are needed to establish the mechanism of the relaxivity enhancement of Gd-DTPA/DACHPt–loaded micelles, and they are currently under way in our laboratory.

The construction of macromolecular MRI contrast agents has been an attractive strategy to achieve diagnostic agents with extended blood circulation. Nevertheless, for Gd-based contrast agents, this approach could increase the risk of toxicity due to the prolonged tissue exposure to those macromolecules and the potential release of Gd^{3+} ions. Thus, the accumulation of high-generation dendrimer contrast agents in the healthy tissues might potentiate the nephrotoxicity and hepatotoxicity risks (37). Accordingly, only 20% of the injected dose of a generation 4–based PAMAM-Gd contrast agent was excreted from the body during the first 2 days, showing transient accumulation in the renal tubules. In contrast to this, the biodistribution of
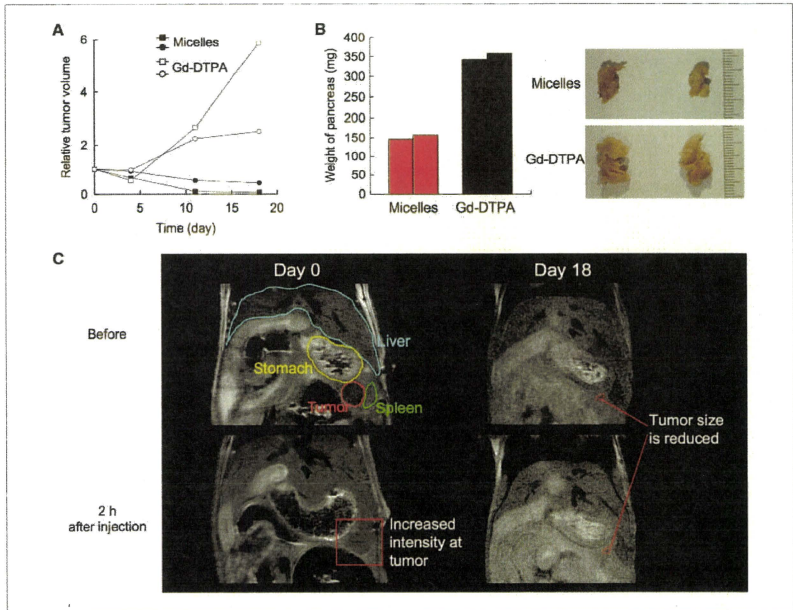

Figure 5. *In vivo* antitumor activity of Gd-DTPA/DACHPt–loaded micelles on orthotopic pancreatic cancer model (BxPC3) assessed by volumetric MRI. A, effect of Gd-DTPA/DACHPt–loaded micelles (8 mg/kg on Pt basis) and Gd-DTPA (30 mg/kg) injected i.v. at day 0, 4, 11 and 18 on the growth of BxPC3 tumors. B, left, weight of the whole pancreas for mice treated with the micelles or Gd-DTPA at day 18 on the antitumor experiment; right, macroscopies of the excised pancreas after treatment with the micelles or Gd-DTPA. C, MRI at days 0 and 18 of a tumor-bearing mouse treated with Gd-DTPA/DACHPt–loaded micelles. The tumor size was 89 mm^3 at day 0 and 5 mm^3 at day 18.
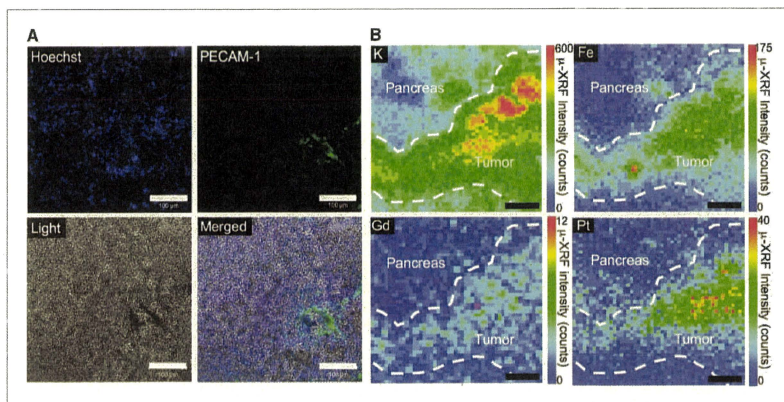
Figure 6. Intratumoral distribution of Gd-DTPA/DACHPt–loaded micelles in orthotopic BxPC3 tumors. A, immunofluorescence microscopy of tumor sections 4 h after injection of the micelles. The cell nuclei were stained with Hoechst, and the blood vessels were marked with PECAM-1 antibody. Scale bars, 100 μm. B, K, Fe, Pt, and Gd distribution in a tumor section including normal pancreatic tissue determined by μ-SR-XRF. Scale bars, 100 μm.

Gd-DTPA/DACHPt–loaded micelles revealed minimal accumulation of Gd-DTPA in normal tissues. Moreover, the Gd-DTPA released from the micelles probably is rapidly excreted from the body because of the relatively fast plasma clearance of low–molecular weight Gd-DTPA, thus eliminating the risk of undesired toxicity.

The real-time observation of drug distribution can increase the accuracy of treatment and enable practitioners to obtain feedback on the therapeutic efficacy at an earlier stage, and promptly adjust the treatment strategy. Gd-DTPA/DACHPt–loaded micelles might be helpful for directly assessing the distribution of the anticancer drugs at early stages by MRI. In this study, the μ-XRF results showed that the delivered Gd-DTPA and DACHPt were colocalized and uniformly distributed within the pancreatic tumors, whereas there was no drug accumulation in healthy pancreas, supporting the strong diagnostic and anticancer effect of the micelles (Fig. 6B, Pt and Gd). Moreover, the chemotherapy regimens are given in periodic cycles, for example, one cycle every 2 weeks during 12 weeks in FOLFOX (folinic acid, fluorouracil, and oxaliplatin) regimen for the treatment of colorectal cancer. By using Gd-DTPA/DACHPt–loaded micelles, the tumor size can be followed up in real-time by imaging at the day of the drug administration. Consequently, the

Gd-DTPA/DACHPt–loaded micelles will have significant implications in the design and development of advanced multifunctional nanomedicines with great potential for clinical application as visible DDS.

Disclosure of Potential Conflicts of Interest

No potential conflicts of interest were disclosed.

Acknowledgments

Grant Support

References

1. Inoue A, Saijo Y, Maemondo M, et al. Severe acute interstitial pneumonia and gefitinib. Lancet 2003;361:137–9.
2. Jones BL. Trastuzumab: hopes and realities. Lancet Oncol 2002;3: 137–44.
3. Ewer MS, Vooletich MT, Durand JB, et al. Reversibility of trastuzu-mab-related cardiotoxicity: new insights based on clinical course and response to medical treatment. J Clin Oncol 2005;23:7820–6.
4. Scappaticci FA, Skillings JR, Holden SN, et al. Arterial thromboembolic events in patients with metastatic carcinoma treated with chemotherapy and bevacizumab. J Natl Cancer Inst 2007;99:1232–9.

5. Davis ME, Chen Z, Shin DM. Nanoparticle therapeutics: an emerging treatment modality for cancer. Nat Rev Drug Discov 2008;7: 771–82.
6. Torchilin VP. Recent advances with liposomes as pharmaceutical carriers. Nat Rev Drug Discov 2005;4:145–60.
7. Peer D, Karp JM, Hong S, Farokhzad OC, Margalit R, Langer R. Nanocarriers as an emerging platform for cancer therapy. Nature Nanotech 2007;2:751–60.
8. Ferrari M. Cancer nanotechnology: opportunities and challenges. Nat Rev Cancer 2005;5:161–71.
9. Duncan R. Polymer conjugates as anticancer nanomedicines. Nat Rev Cancer 2006;6:688–701.
10. Kabanov AV, Alakhov VY. Pluronic block copolymers in drug delivery: from micellar nanocontainers to biological response modifiers. Crit Rev Ther Drug Carrier Syst 2002;19:1–73.
11. Nishiyama N, Kataoka K. Current state, achievements, and future prospects of polymeric micelles as nanocarriers for drug and gene delivery. Pharmacol Ther 2006;112:630–48.
12. Matsumura Y, Kataoka K. Preclinical and clinical studies of anticancer agent-incorporating polymer micelles. Cancer Sci 2009;100:572–9.
13. Hashizume H, Baluk P, Morikawa S, et al. Opening between defective endothelial cells explain tumor vessel leakiness. Am J Pathol 2000;156:1363–80.
14. Maeda H. The enhanced permeability and retention (EPR) effect in tumor vasculature: the key role of tumor-selective macromolecular drug targeting. Adv Enzyme Regul 2001;41:189–207.
15. Muggia FM, Hainsworth JD, Jeffers S, et al. Phase II study of liposomal doxorubicin in refractory ovarian cancer: antitumor activity and toxicity mediated by liposomal encapsulation. J Clin Oncol 1997; 15:987–93.
16. Gradishar WJ, Tjulandin S, Davidson N, et al. Phase III trial of nanoparticle albumin-bound paclitaxel compared with polyethylated castor oil-based paclitaxel in women with breast cancer. J Clin Oncol 2005;23:7794–803.
17. Matsumura Y, Maeda H. A new concept for macromolecular therapeutics in cancer chemotherapy: mechanism of tumoritropic accumulation of proteins and the antitumor agent SMANCS. Cancer Res 1986;46:6387–92.
18. Hamaguchi T, Matsumura Y, Shirao K, et al. Phase I study of novel drug delivery system, NK911, a polymer micelle encapsulated doxorubicin [abstract 571]. Proceedings of the 39th annual meeting of the American Society of Clinical Oncology (ASCO); 2003, May 31-June 3; Chicago, USA.
19. Kato K, Hamaguchi T, Yasui H, et al. Phase I study of NK105, a paclitaxel-incorporating micellar nanoparticle, in patients with advanced cancer. ASCO Annual Meeting Proceedings. J Clin Oncol 2006;24:2018.
20. Burris HA III, Infante JR, Spigel DR, et al. A phase I dose-escalation study of NK012. ASCO Annual Meeting Proceedings. J Clin Oncol 2008;26:2538.
21. Wilson RH, Plummer R, Adam J, et al. Phase I and pharmacokinetic study of NC-6004, a new platinum entity of cisplatin-conjugated polymer forming micelles. J Clin Oncol 2008;26:2573.
22. Dent R, Trudeau M, Pritchard KI, et al. Triple-negative breast cancer: clinical features and patterns of recurrence. Clin Cancer Res 2007; 13:4429–34.
23. McCarthy JR, Weissleder R. Multifunctional magnetic nanoparticles for targeted imaging and therapy. Adv Drug Deliv Rev 2008;60: 1241–51.
24. McCarthy JR, Jaffer FA, Weissleder R. A macrophage-targeted theranostic nanoparticle for biomedical applications. Small 2006; 2:983–7.
25. Pan D, Caruthers SD, Hu G, et al. Ligand-directed nanobialys as theranostic agent for drug delivery and manganese-based magnetic resonance imaging of vascular targets. J Am Chem Soc 2008;130: 9186–7.
26. Nasongkla N, Bey E, Ren J, et al. Multifunctional polymeric micelles as cancer-targeted, MRI-ultrasensitive drug delivery systems. Nano Lett 2006;6:2427–30.
27. Weinmann HJ, Brasch RC, Press WR, Wesbey GE. Characteristics of gadolinium-DTPA complex: a potential NMR contrast agent. Am J Roentgenol 1984;142:619–24.
28. Cabral H, Nishiyama N, Okazaki S, Koyama H, Kataoka K. Preparation and biological properties of dichrolo(1,2-diaminocyclohexane) platinum(II) (DACHPt)-loaded polymeric micelles. J Control Release 2005;101:223–32.
29. Gouin S, Winnik F. Quantitative assays of the amount of diethylenetriaminepentaacetic acid conjugated to water-soluble polymers using isothermal titration calorimetry and colorimetry. Bioconjug Chem 2001;12:372–7.
30. Terada Y, Goto S, Takimoto N, et al. Construction and commissioning of BL37XU at SPring-8. AIP Conf Proc 2004;705:376–9.
31. Ventrucci M, Cipolla A, Racchini C, Casadei R, Simoni P, Gullo L. Tumor M2-pyruvate kinase, a new metabolic marker for pancreatic cancer. Dig Dis Sci 2004;49:1149–55.
32. Jemal A, et al. Cancer statistics, 2007. CA Cancer J Clin 2007;57: 43–66.
33. Sofuni A, et al. Differential diagnosis of pancreatic tumors using ultrasound contrast imaging. J Gastroenterol 2005;40:518–25.
34. Miller FH, Rini NJ, Keppke AL. MRI of adenocarcinoma of the pancreas. Am J Roentgenol 2006;187:W365–374.
35. Zhang Z, Greenfield MT, Spiller M, McMurry TJ, Lauffer RB, Caravan P. Multilocus binding increases the relaxivity of protein-bound MRI contrast agents. Chem 2005;117:6924–7.
36. Livramento JB, Toth E, Sour A, Borel A, Merbach AE, Ruloff R. High relaxivity confined to a small molecular space: a metallostar-based potential MRI contrast agent. Angew Chem Int Ed 2005; 44:1480–4.
37. Duncan R, Izzo L. Dendrimer biocompatibility toxicity. Adv Drug Deliv Rev 2005;57:2215–37.

Direct and instantaneous observation of intravenously injected substances using intravital confocal micro-videography

Yu Matsumoto,[1,2,3] Takahiro Nomoto,[4] Horacio Cabral,[4] Yoko Matsumoto,[5]
Sumiyo Watanabe,[1,6,7] R. James Christie,[8] Kanjiro Miyata,[1] Makoto Oba,[9]
Tadayoshi Ogura,[10] Yuichi Yamasaki,[8] Nobuhiro Nishiyama,[1] Tatsuya Yamasoba,[2]
and Kazunori Kataoka[1,4,8,*]

[1]Division of Clinical Biotechnology, Center for Disease Biology and Integrative Medicine,
Graduate School of Medicine, The University of Tokyo, Japan
[2]Department of Otorhinolaryngology and Head and Neck Surgery,
Graduate School of Medicine and Faculty of Medicine, The University of Tokyo, Japan
[3]Department of Otorhinolaryngology and Head and Neck Surgery, Mitsui Memorial Hospital, Japan
[4]Department of Bioengineering, Graduate School of Engineering, The University of Tokyo, Japan
[5]Department of Obstetrics and Gynecology, Graduate School of Medicine and Faculty of Medicine,
The University of Tokyo, Japan
[6]Division of Nephrology and Endocrinology, Department of Internal Medicine,
Graduate School of Medicine and Faculty of Medicine, The University of Tokyo, Japan
[7]Department of Internal Medicine, Teikyo University School of Medicine, Japan
[8]Department of Materials Engineering, Graduate School of Engineering, The University of Tokyo, Japan
[9]Department of Vascular Regeneration, Division of Tissue Engineering, The University of Tokyo Hospital, Japan
[10]Nikon Instech Co., Ltd., Japan
*kataoka@bmw.t.u-tokyo.ac.jp

Abstract: We describe the development and application of intravital confocal micro-videography to visualize entrance, distribution, and clearance of drugs within various tissues and organs. We use a Nikon A1R confocal laser scanning microscope system attached to an upright ECLIPSE FN1. The Nikon A1R allows simultaneous four channel acquisition and speed of 30 frames per second while maintaining high resolution of 512 × 512 scanned points. The key techniques of our intravital imaging are (1) to present a flat and perpendicular surface to the objective lens, and (2) to expose the subject with little or no bleeding to facilitate optical access to multiple tissues and organs, and (3) to isolate the subject from the body movement without compressing the blood vessels, and (4) to insert a tail vein catheter for timed injection without moving the subject. Ear lobe dermis tissue was accessible without surgery. Liver, kidney, and subcutaneous tumor were accessed following exteriorization through skin incision. In order to image initial extravasations of compounds into tissue following intravenous injection, movie acquisition was initialized prior to drug administration. Our technique can serve as a powerful tool for investigating biological mechanisms and functions of intravenously injected drugs, with both spatial and temporal resolution.

© 2010 Optical Society of America

OCIS codes: (170.1790) Confocal microscopy; (170.2655) Functional monitoring and imaging.

References and links

1. I. Veilleux, J. A. Spencer, D. P. Biss, D. Cote, and C. P. Lin, "In Vivo Cell Tracking With Video Rate Multimodality Laser Scanning Microscopy," IEEE J. Sel. Top. Quantum Electron. 14(1), 10–18 (2008).
2. P. Kim, M. Puoris'haag, D. Côté, C. P. Lin, and S. H. Yun, "In vivo confocal and multiphoton microendoscopy," J. Biomed. Opt. 13(1), 010501 (2008).
3. P. Kim, E. Chung, H. Yamashita, K. E. Hung, A. Mizoguchi, R. Kucherlapati, D. Fukumura, R. K. Jain, and S. H. Yun, "In vivo wide-area cellular imaging by side-view endomicroscopy," Nat. Methods 7(4), 303–305 (2010).
4. R. Mehvar, M. A. Robinson, and J. M. Reynolds, "Molecular weight dependent tissue accumulation of dextrans: in vivo studies in rats," J. Pharm. Sci. 83(10), 1495–1499 (1994).

5. R. Mehvar, and T. L. Shepard, "Molecular-weight-dependent pharmacokinetics of fluorescein-labeled dextrans in rats," J. Pharm. Sci. **81**(9), 908–912 (1992).
6. G. Zhang, V. Budker, and J. A. Wolff, "High levels of foreign gene expression in hepatocytes after tail vein injections of naked plasmid DNA," Hum. Gene Ther. **10**(10), 1735–1737 (1999).
7. F. Liu, Y. Song, and D. Liu, "Hydrodynamics-based transfection in animals by systemic administration of plasmid DNA," Gene Ther. **6**(7), 1258–1266 (1999).
8. H. Herweijer, and J. A. Wolff, "Progress and prospects: naked DNA gene transfer and therapy," Gene Ther. **10**(6), 453–458 (2003).
9. D. Liu, and J. E. Knapp, "Hydrodynamics-based gene delivery," Curr. Opin. Mol. Ther. **3**(2), 192–197 (2001).
10. A. Crespo, A. Peydró, F. Dasí, M. Benet, J. J. Calvete, F. Revert, and S. F. Aliño, "Hydrodynamic liver gene transfer mechanism involves transient sinusoidal blood stasis and massive hepatocyte endocytic vesicles," Gene Ther. **14**(11), 927–935 (2005).
11. T. Suda, X. Gao, D. B. Stolz, and D. Liu, "Structural impact of hydrodynamic injection on mouse liver," Gene Ther. **14**(2), 129–137 (2007).
12. G. Zhang, X. Gao, Y. K. Song, R. Vollmer, D. B. Stolz, J. Z. Gasiorowski, D. A. Dean, and D. Liu, "Hydroporation as the mechanism of hydrodynamic delivery," Gene Ther. **11**(8), 675–682 (2004).
13. Y. Ohno, H. Birn, and E. I. Christensen, "In vivo confocal laser scanning microscopy and micropuncture in intact rat," Nephron, Exp. Nephrol. **99**(1), e17–e25 (2005).

Introduction

In vivo imaging has received much attention in recent years, as it can elucidate the complex biological and pathological events within a living animal. Although histological examination of excised tissues has long served as a fundamental approach for tissue analysis, intravital confocal microscopy provides instant histopathology at the cellular and subcellular level and therefore is ideal for investigating dynamic events involved. Here we describe the development and application of intravital confocal micro-videography to visualize entrance, distribution, and clearance of drugs within various tissues and organs. In order to image initial extravasations of compounds into tissue following intravenous injection, movie acquisition was initialized prior to drug administration. Many groups have adapted commercial confocal microscopes for intravital imaging, but they often use conventional galvano scanners with slow acquisition speed. Progressive groups build confocal and/or multi-photon microscopes and even microendoscopes with rapid scanning systema in-house to achieve video-rate imaging [1–3].

Table 1. Commercially available rapid scanning confocal microscopes

Vendor	Product Name	Scanning System	Maximum Frame Rate at 512 x 512 Pixels	Number of Simultaneously Detectable Channels
Nikon	A1R	Resonant Scanner	30 fps	4
Leica Microsystems	TCS SP5 II	Resonant Scanner	25 fps	5
Carl Zeiss	LSM 7 LIVE	Linear Scanner	120 fps	2
Yokogawa Electric	CSU-X1	Nipkow spinning disk	2000 fps	3
Olympus	DSU	Spinning Disk Confocal	15 fps	1

Recently, several rapid scanning confocal microscopes became commercially available (Table 1). Although all vendors primarily recommend use of their products with an inverted configuration (optimized for live cell imaging), combination with an upright microscope has advantages for intravital imaging. Here, we attached a Nikon A1R confocal laser scanning microscope system to an upright ECLIPSE FN1 to acquire video images. The A1R incorporates both a conventional galvano scanner and also a high-speed resonant scanner, which allows an acquisition speed of 30 frames per second and simultaneous four channel detection, while maintaining high resolution of 512×512 scanned points.Our technique consists of the following essential features:

(1) Front-end design presenting a flat and perpendicular surface against the objective lens;

(2) Exposure surgery with little or no bleeding to facilitate optical access to multiple tissues and organs;

(3) Stabilization of the sample to isolate from the body movement without compressing the blood vessels;

(4) Tail vein catheterization for timed injection during data acquisition, without moving the subject;

Our technique is particularly effective for investigating the dynamic and complex events that occur immediately following drug administration. We investigated the influence of molecular weight on pharmacokinetic behavior by imaging the ear lobe dermis. We also investigated the accumulation of pDNA within liver tissue by hydrodynamic injection. Kidney and tumor tissues were imaged to observe renal excretion and tumor extravasation.

Results and discussion

During the development of a promising drug delivery system, there is a strong need to accurately grasp the intravital behavior of the administered drugs [4,5]. We investigated the influence of molecular weight on pharmacokinetic behavior using fluorescein (MW = 332) and fluorescein-labeled dextrans (FD) with average molecular weights of 10-, 40-, and 500 kDa (Fig. 1). Fluorescein and FDs demonstrated different pharmacokinetics [Fig. 1(c), 1(e), Media 1, Media 2, Media 3, and Media 4]. Arterial entrance was observed 10 seconds after injection, followed by venous migration 30 seconds after injection. Fluorescein diffused into extravascular tissue concurrently with venous migration. FD 10 kDa gradually translocated into extravasculature tissue 10-15 minutes after injection and lymphatic drainage was observed after 20 minutes. FD 70- and 500 kDa remained in the vasculature during the entire 60-minute observation period. Our confocal micro-videography technique is superior to conventional methods used to study plasma clearance in regard to the number of animals needed to generate a clearance curve and also the ability to obtain more information from a single experiment. Conventional protocols used in plasma clearance studies require blood extraction at various post-injection time points, using multiple animals. In contrast, intravital confocal micro-videography yields 30 time points per seconds before, during, and after the injection. Moreover, our technique provides spatial resolution so that we can individually investigate multiple regions such as arteries, veins, extravascular tissue, lymphatic vessels, and even cells and nuclei if desirable [Fig. 1(d)]. For long-term plasma clearance studies, however, we still perform conventional methods in conjunction with our technique because prolonged anesthesia periods longer than five hours are not practical.
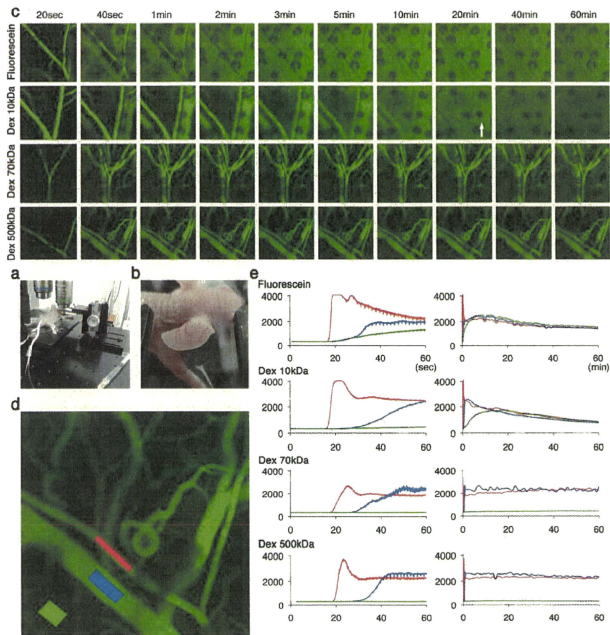
Fig. 1. (a) The earlobe is an excellent location for intravital confocal micro-videography because blood vessels are easily observed in the dermis and the ear is easily accessed and positioned in the imaging apparatus. (b) Earlobe was attached to the coverslip with a small drop of immersion oil. (c) Fluorescein, FD 10-, 70-, and 500 kDa were administered via tail vein catheter 10 seconds after movie acquisition was initiated. Video-rate (30 fps) movies were recorded for the first minute, and subsequent time-lapse images were recorded every minute for an additional 60 minutes. The arrow indicates lymphatic drainage. Obtained data sets were further processed using Nikon NIS-Elements C software. Image size: 645.50μm x 645.50μm. (d) Three regions of interest (ROI) are selected respectively as an artery (red), vein (blue), and extravascular skin tissue (green). Image size: 645.50μm x 645.50μm. (e) Fluorescence intensity in these ROIs plotted against time. All movies are provided as supplementary movie files (Media 1, Media 2, Media 3, and Media 4).

The liver is a vital organ that has a wide range of functions, including detoxification, protein synthesis, storage, and production of bile. Real-time imaging of liver dynamics and small changes in hepatocytes will provide insight to poorly understood processes that occur in the liver. We applied our real-time imaging technique to observe the accumulation of pDNA within liver tissue by hydrodynamic injection [Fig. 2(a)]. Delivery of pDNA by hydrodynamic injection involves rapid tail vein injection of a large volume of pDNA solution and efficient accumulation of pDNA in the liver is reported [6,7]. This method has been widely utilized by the gene therapy community for evaluating therapeutic activities of various genes [8,9].

Following normal injection, pDNA flowed into the hepatic lobule from the hepatic artery, through the sinusoids, and towards the central vein (Media 5). After 20 minutes, pDNA was observed adjacent to vessel walls, but was rarely transferred into hepatic cells. In contrast, hydrodynamic injection of pDNA resulted in initial flow into the hepatic lobule from the hepatic artery, but the flow stopped at the sinusoids. After 50 seconds, pDNA appeared from the central vein, indicating retrodynamic blood flow. Blood flow oscillated back and forth within the sinusoids, indicating that the blood pressure of central and portal vein remained in equilibrium, which lasted as long as 3 minutes (Media 6). During the 30-minute period after injection, pDNA was observed in more hepatic cell nuclei by hydrodynamic injection than normal injection. It has been hypothesized that hydrodynamic injection generates retrodynamic blood flow from the central vein [10–12]. This hypothesis was well described by performing dual pressure detector system of the portal vein and inferior vena cava, and is further supported by our results obtained by direct imaging of the hepatic lobule.
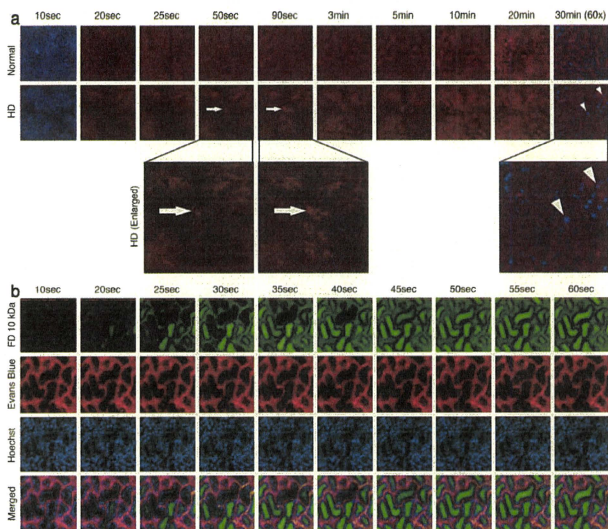

Fig. 2. (a) Intravital confocal micro-videography of the mouse hepatic lobule. Hoechst (blue) was intravenously injected 15 minutes before imaging. Cy5-labeled pDNA (red) were normally or hydrodynamically (HD) injected via tail vein catheter 10 seconds after movie acquisition was initiated (Media 5 and Media 6). Image frames were extracted from both videos at identical time points for comparison. Image size: 645.50μm x 645.50μm. Zoomed pictures were taken 30 minutes after injection. Image size: 212.13μm x 212.13μm. Hoechst channels are shown at 10 sec and 30 min for histological comprehension. Arrows indicate reverse blood flow from central vein. Arrowheads indicate nuclei that pDNA were successfully transferred. (b) Intravital confocal micro-videography of mouse kidney tissue. Hoechst (blue) and Evan's Blue dye (red) were intravenously injected 15 minutes and 5 minutes before imaging, respectively. FD 10 kDa (green) were administered via tail vein catheter 10 seconds after movie acquisition was initiated (Media 7). Image size: 645.50μm x 645.50μm.

To further demonstrate the feasibility of our technique, kidney and tumor tissues were imaged to observe renal excretion and tumor extravasation. Deeper kidney structures such as glomeruli could not be imaged because renal tissue highly absorbs and scatters light [13]. Although the imaging of the renal cortex was limited to shallow features such as proximal and distal tubules and capillary vessels, we still could evaluate glomerular filtration indirectly [Fig. 2(b)]. FD 10 kDa flowed into the capillary blood vessels and proximal tubules at the same time, which indicate that FD 10 kDa were immediately filtered by glomerulus. FD 10 kDa flowed into the distal tubules shortly afterward, until all the tubules were filled. The albumin - Evan's blue dye complex remained in blood circulation throughout the study for 60 minutes. Observation of the albumin - Evan's blue dye complex also depicted tumor vasculature [Fig. 3(a)]. Multiple frames were merged to produce a wide-area image [Fig. 3(b)].
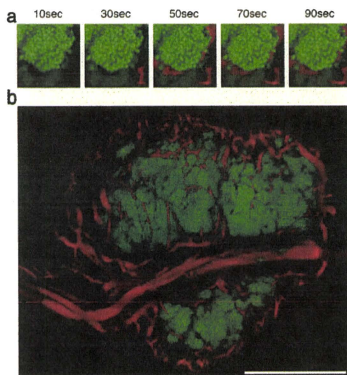

Fig. 3. (a) Intravital confocal micro-videography of subcutaneous HeLaˢH2BGFP tumor. Evan's blue dye was administered via tail vein catheter 10 seconds after movie acquisition was initiated. Image frames were extracted from the video at indicated time points. Image size: 212.13μm x 212.13μm (b) Motorized XY stage enables 'large image acquisition' feature of the Nikon NIS-Elements C software. Multiple frames were automatically captured in sequence and merged to produce a wide-area image. Scale bar: 1 mm.

Arterial entrance, venous migration, extravasation into tissue, and clearance was directly observed within various tissues and organs. The intravital confocal micro-videography technique described here is useful for investigating biological mechanisms and functions in both spatial and temporal resolution. Our technique is particularly effective for investigating the dynamic and complex events that occur immediately following drug administration, such as first path effects, site-specific drug accumulation, blood circulation and metabolism behavior.

Materials and methods

Microscope

All picture/movie acquisitions were performed using a Nikon A1R confocal laser scanning microscope system attached to an upright ECLIPSE FN1 (Nikon Corp., Tokyo, Japan). The A1R incorporates both conventional a galvano scanner and also a high-speed resonant scanner. The resonant scanner allows an acquisition speed of 30 frames per second while

maintaining high resolution of 512 × 512 scanned points. Modification of the ECLIPSE FN1 was necessary for intravital imaging because this upright microscope is originally designed for imaging thin, sectioned slices, and not for live animals. The trans-illumination unit (halogen lamp, condenser, sub-stage and turret) was removed entirely from the microscope, as confocal imaging never requires transmitted light, which allowed for more space between the microscope stage and the objective lens. The motorized stage was set as low as possible onto a customized framework, and a custom-designed height-adjustable mouse stage was fixed onto the motorized stage. Small temperature controller (Thermoplate; Tokai Hit Co., Ltd., Shizuoka, Japan) was integrated to the mouse stage [Fig. 1(a)]. For sample imaging, a custom-designed height adjustable coverslip holder is placed onto the tissue of interest to provide a flat surface for the objective lens [Fig. 1(b)]. The coverslip must be perpendicular to the objective lens, tightly fixed, and rigid enough so that the tissue of interest will not move during the imaging, but not so tight as to restrict blood flow. The detailed blueprint of the custom-designed mouse stage and the coverslip holder (fabricated and assembled by Sigma Koki Co. Ltd., Tokyo, Japan) will be provided upon request.

Fluorescent reagents

Hoechst 33342 dye (8 mg/kg in PBS, Lonza Group Ltd., Basel, Switzerland) was used to stain the nuclei of cells present in circulation and in the perivascular space. Evans Blue dye (8 mg/kg in PBS, Wako Pure Chemical Industries, Ltd., Osaka, Japan), which binds to plasma albumin, was used to stain the vasculature. Fluorescein (4 mg/kg in PBS, molecular weight of 332.31, Alcom Japan, Ltd., Tokyo, Japan) and fluorescein-labeled dextrans with average molecular weights of 10k, 70k, 500k (Invitrogen Corporation, Carlsbad, CA, USA) were used to study molecular weight-dependent pharmacokinetics. For the comparison study of normal and hyrodynamic injection, psFLT-1 plasmid DNA was labeled with Cy5 using Label IT Tracker Nucleic Acid Localization Kits (Mirus Bio Corporation, Madison, WI, USA).

Surgical procedures

All animal experimental procedures were executed in accordance with the Guide for the Care and Use of Laboratory Animals as stated by the National Institutes of Health. Mice were anesthetized with 2.0-3.0% isoflurane (Abbott Japan Co., Ltd., Tokyo, Japan) using a Univenter 400 Anaesthesia Unit (Univentor Ltd., Zejtun, Malta). Mice were then subjected to lateral tail vein catheterization with a 30-gauge needle (Becton, Dickinson and Co, Franklin Lakes, NJ, USA) connected to a non-toxic, medical grade polyethylene tube (Natsume Seisakusho Co., Ltd., Tokyo, Japan). Catheterization technique is described elsewhere (http://imaging.bme.ucdavis.edu/surgical.html). This catheterization allows multiple and timed injection without moving the mouse during data acquisition.

Ear lobe dermis tissue was accessible without surgery and easily fixed beneath the cover slip with a single drop of immersion oil. Tumor, kidney, or liver tissues were accessed following exteriorization through skin incision. For tumor imaging, female BALB/c nude mice were inoculated subcutaneously with H2B-GFP cells, which express green fluorescence protein in cell nuclei. Tumors were allowed to mature until the size of the tumor reached 5 mm in diameter. To minimize bleeding during the surgical procedure required to present tumors for imaging, a Surgitron (R) radio-frequency surgical device equipped with a Vari-Tip (TM) Wire Electrode (Cat. No. A8D) (Ellman International Inc., Oceanside, NY, USA) was used for bloodless, micro smooth incision with minimal tissue alteration.

Movie and time-lapse image acquisition

Video acquisition at a speed of 30 frames per second was performed for the indicated times, followed by time-lapse imaging every 1 minute. Drugs were administered via the tail vein catheter 10 seconds after video acquisition was initiated.

Biomaterials

ELSEVIER

Polyplex micelles prepared from ω-cholesteryl PEG-polycation block copolymers for systemic gene delivery

Makoto Oba [a], Kanjiro Miyata [b], Kensuke Osada [c], R. James Christie [c], Mai Sanjoh [d], Weidong Li [c], Shigeto Fukushima [c], Takehiko Ishii [d], Mitsunobu R. Kano [b,e], Nobuhiro Nishiyama [b], Hiroyuki Koyama [a], Kazunori Kataoka [b,c,d,*]

[a] Department of Clinical Vascular Regeneration, Graduate School of Medicine, The University of Tokyo, 7-3-1 Hongo, Bunkyo-ku, Tokyo 113-8655, Japan
[b] Center for Disease Biology and Integrative Medicine, Graduate School of Medicine, The University of Tokyo, 7-3-1 Hongo, Bunkyo-ku, Tokyo 113-0033, Japan
[c] Department of Materials Engineering, Graduate School of Engineering, The University of Tokyo, 7-3-1 Hongo, Bunkyo-ku, Tokyo 113-8656, Japan
[d] Department of Bioengineering, Graduate School of Engineering, The University of Tokyo, 7-3-1 Hongo, Bunkyo-ku, Tokyo 113-8656, Japan
[e] Department of Molecular Pathology, Graduate School of Medicine, The University of Tokyo, 7-3-1 Hong, Bunkyo-ku, Tokyo 113-8655, Japan

ABSTRACT

Polyplex micelles formed with plasmid DNA (pDNA) and poly(ethylene glycol) (PEG)-block-poly{N-[N-(2-aminoethyl)-2-aminoethyl]aspartamide} [PAsp(DET)] exhibit effective endosomal escaping properties based on di-protonation of diamine side chains with decreasing pH, which improves their transfection efficiency and thus are promising candidates for local in vivo gene transfer. Here, PEG-PAsp(DET) polyplex micelles were further improved as in vivo systemic vectors by introduction of cholesterol (Chole) into the ω-terminus of PEG-PAsp(DET) to obtain PEG-PAsp(DET)-Chole. Introduction of the cholesterol resulted in enhanced association of block copolymers with pDNA, which led to increased stability in proteinous medium and also in the blood stream after systemic injection compared to PEG-PAsp(DET) micelles. The synergistic effect between enhanced polymer association with pDNA and increased micelle stability of PEG-PAsp(DET)-Chole polyplex micelles led to high in vitro gene transfer even at relatively low concentrations, due to efficient cellular uptake and effective endosomal escape of block copolymers and pDNA. Finally, PEG-PAsp(DET)-Chole micelles achieved significant suppression of tumor growth following intravenous injection into mice bearing a subcutaneous pancreatic tumor using therapeutic pDNA encoding an anti-angiogenic protein. These results suggest that PEG-PAsp(DET)-Chole micelles can be effective systemic gene vectors for treatment of solid tumors.

© 2010 Elsevier Ltd. All rights reserved.

1. Introduction

As expectations for gene therapy increase, so have efforts to develop non-viral vectors with high transfection ability and low toxicity [1,2]. Polyplexes, which are composed of polycations and plasmid DNA (pDNA), are expected as alternatives to viral vectors due to the fine-tuned properties for specific applications by altering the structure of the polycation used for polyplex formation [3–5]. Polyplex micelles formed with poly(ethylene glycol) (PEG)-block-polycation block copolymers and pDNA are particularly promising candidates [6–8], due to their excellent

characteristics as in vivo gene vectors [9,10]. The biocompatible PEG shell layer surrounding the polyplex core contributes to high colloidal stability, allows micelles to maintain their initial size of approximately 100 nm, and reduces non-specific interactions with blood components, which are all desirable properties for systemic administration.

Recently, we reported that polyplex micelles prepared with pDNA and PEG-block-poly{N-[N-(2-aminoethyl)-2-aminoethyl] aspartamide} [PEG-PAsp(DET)] [11] achieved successful in vitro transfection of primary cells due to effective endosomal escape of pDNA contained in the micelle core. The PAsp(DET), polycationic segment of the block copolymer is characterized by a distinctive two-step protonation behavior in response to pH and possessed endosomal membrane-selective destabilizing capacity upon acidification [12]. Furthermore, PEG-PAsp(DET) polyplex micelles have shown successful in vivo gene transfer by local administration in

* Corresponding author. Department of Materials Engineering, Graduate School of Engineering, The University of Tokyo, 7-3-1 Hongo, Bunkyo-ku, Tokyo 113-8656, Japan. Tel.: +81 3 5841 7138; fax: +81 3 5841 7139.
E-mail address: kataoka@bmw.t.u-tokyo.ac.jp (K. Kataoka).

several animal models including: a clamped rabbit carotid artery with neointima without vessel occlusion by thrombus [13], a mouse skull by regulated release from a calcium phosphate cement scaffold to induce bone regeneration through the osteogenic factors [14], and a rat lung pulmonary arterial hypertension model via intratracheal administration [15]. In these cases, however, excess block copolymers relative to pDNA (high N/P ratio) were required to achieve high transfection efficiency, suggesting the existence of free polymer. If free polymer plays a significant role for gene transfer with polyplex micelles prepared from PEG-PAsp (DET) and pDNA, the transfection efficiency under highly diluted conditions, such as systemic application, could be drastically decreased.

The aim of this study was to further develop PEG-PAsp(DET) polyplex micelles towards in vivo systemic pDNA delivery vectors. In order to enhance the association of PEG-PAsp(DET) polymers with pDNA and thus increase the efficiency of cellular internalization of polymer necessary for improved endosome escaping, we utilized both electrostatic interaction between polycations and pDNA and hydrophobic interaction by cholesterol to form micelles with improved stability. Specifically, cholesterol was introduced onto the ω-terminus of the PAsp(DET) segment in PEG-PAsp(DET) block copolymer. Cholesterol introduction significantly increased the number of block copolymers associating with a pDNA. In vitro experiments were done to demonstrate improved transfection efficiency of PEG-PAsp(DET)-Chole polyplex micelles at low N/P ratios and under the diluted conditions compared to the control micelles formed without cholesterol modified block copolymer. Then, the enhanced stability by the cholesterol introduction in blood was shown, thus allowing successful treatment of a subcutaneous tumor by systemic administration of micelles prepared with PEG-PAsp(DET)-Chole and therapeutic pDNA encoding for an anti-angiogenic protein.

2. Materials and methods

2.1. Materials

Dichloromethane (CH$_2$Cl$_2$), N,N-dimethylformamide (DMF), triethylamine (TEA), and 3-(4,5-dimethylthiazol-2-yl)-2,5-diphenyltetrazolium bromide (MTT) were purchased from Wako Pure Chem. Co. Ltd. (Osaka, Japan). Cholesterol chloroformate was purchased from Aldrich Chemical Co. Ltd. (Milwaukee, WI). Diethylenetriamine (DET) was purchased from Tokyo Kasei Kogyo (Tokyo, Japan) and distilled over CaH$_2$ under reduced pressure. DMF was dehydrated using activated molecular sieves (4A) and distilled under reduced pressure. PEG-PAsp(DET) block copolymer (PEG: 12,000 g/mol, polymerization degree of PAsp(DET) segment: 68) was synthesized as previously reported [11]. Alexa Fluor 680 (Alexa680) succinimidyl ester was a product of Invitrogen (Carlsbad, CA). A Micro BCA protein assay reagent kit was purchased from Pierce (Rockford, IL). The Luciferase assay kit was a product of Promega (Madison, WI). Plasmid pCAcc+Luc coding for firefly luciferase under the control of the CAG promoter was provided by RIKEN Gene Bank (Tsukuba, Japan), amplified in competent DH5a Escherichia coli, and then purified using a HiSpeed Plasmid MaxiKit purchased from Qiagen Sciences (Germantown, MD). pDNA encoding for a soluble form of VEGF receptor-1 (sFlt-1) was prepared as previously reported [16].

2.2. Animals

Balb/c mice (female, 8 weeks old) and balb/c nude mice (female, 5 weeks old) were purchased from Charles River Laboratories (Tokyo, Japan). All animals were treated in accordance with the guideline of the Animal Ethics Committee of The University of Tokyo.

2.3. Synthesis of α-methoxy-ω-cholesteryl carbamate poly(ethylene glycol)-block-poly[N-[N-(2-aminoethyl)-2-aminoethyl]aspartamide] [PEG-PAsp(DET)]

PEG-b-poly(β-benzyl L-aspartate) (PEG-PBLA) (PEG: 12,000 g/mol, polymerization degree of PBLA segment: 68) was prepared as previously reported [11]. PEG-PBLA (210 mg) was dissolved in CH$_2$Cl$_2$ (4 mL), followed by the addition of 11 v/v% TEA/CH$_2$Cl$_2$ (200 μL) and cholesterol chloroformate (344 mg) in CH$_2$Cl$_2$ (1 mL) at 0 °C. The reaction mixture was stirred at room temperature for 24 h. The reactant polymer was isolated by precipitation into diethylether and lyophilized from
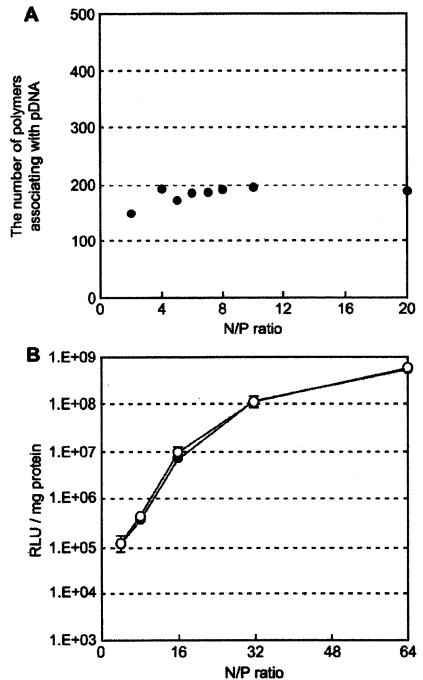
Fig. 1. (A) The number of PEG-PAsp(DET-Alexa680) block copolymers associating with a pDNA. (B) Transfection efficiency of PEG-PAsp(DET) polyplex micelles. Closed circles: addition of polyplex micelle solutions prepared at various N/P ratios into the cell culture medium. Open circles: addition of polyplex micelle solutions prepared at a constant N/P value of 4, with separate addition of PEG-PAsp(DET) free polymer solution into the cell culture medium to obtain the same N/P values shown in the experiment with open circles.

benzene, to obtain PEG-PBLA-Chole (197 mg). PEG-PBLA-Chole (100 mg) was dissolved in DMF (4 mL), followed by reaction with DET (50 equiv. to benzyl group of PBLA segment, 1.43 g) at 40 °C. After 1 h, the reactant mixture was slowly added to a 20% acetic acid (13.8 mL) solution, and subsequently dialyzed against 0.01 N HCl and finally distilled water. The final solution was lyophilized to obtain PEG-PAsp (DET)-Chole (98 mg).

The ^{1}H NMR spectrum of each polymer was obtained with an EX300 spectrometer (JEOL, Tokyo, Japan). Chemical sifts were reported in ppm relative to the residual protonated solvent peak.

2.4. Introduction of Alexa680 into block copolymers

Alexa680 was introduced into the side chains of both PEG-PAsp(DET) and PEG-PAsp(DET)-Chole polymers. The typical synthetic procedure of PEG-PAsp(DET-Alexa680) is described as follows: Alexa680 succinimidyl ester (1 mg) in 100 μL of DMF was added to PEG-PAsp(DET) (30 mg) in 1.5 mL of 0.1 N NaHCO$_3$ (pH 9.3) and stirred at 4 °C for 1 h. The reacted polymer was purified by dialysis against distilled water and lyophilized to obtain PEG-PAsp(DET-Alexa680) (22 mg). Introduction of Alexa680 into PEG-PAsp(DET)-Chole was completed similarly using Alexa680 succinimidyl ester (1 mg) and PEG-PAsp(DET)-Chole (30 mg) to obtain PEG-PAsp(DET-Alexa680)-Chole (23 mg). The number of Alexa680 introduced into the strand of

PEG-PAsp(DET) and PEG-PAsp(DET)-Chole was estimated to be 0.6 and 0.7, respectively, using a spectrofluorometer (ND-3300, NanoDrop, Wilmington, DE).

2.5. Preparation of polyplex micelles

Each block copolymer and pDNA was dissolved separately in 10 mM Tris–HCl buffer (pH 7.4) or 10 mM Hepes buffer (pH 7.3). Polymer solutions of various concentrations were added to a two-fold excess volume of pDNA solution to form polyplex micelles with different compositions. The final pDNA concentration was adjusted to 33.3 μg/mL for in vitro experiments and 100 μg/mL for in vivo experiments and micelle solutions were stored at 4 °C overnight prior to use. The N/P ratio was defined as the residual molar ratio of the amino groups of PAsp(DET) units to the phosphate groups of pDNA. The N⁺/P ratio was defined as the molar ratio of protonated amino groups of PAsp(DET) units to the phosphate groups of pDNA.

2.6. Ultracentrifugation

In order to evaluate the amount of free polymer in the polyplex micelle solution, ultracentrifugation analysis of polyplex micelles, composed of Alexa680-labeled block copolymers and pDNA, was carried out by a Beckman XL-I ultracentrifuge (Beckman Coulter, Inc., Fullerton, CA) using an An-60 Ti 4-hole rotor and standard double-sectors (Epon centerpieces) equipped with quartz windows. The concentration of polyplex micelle solutions prepared at various N/P ratios were adjusted to 33.3 μg pDNA/mL in 10 mM Hepes buffer (pH 7.3). Formation of polyplex micelles was confirmed by UV absorbance measurement at 260 nm, while that of Alexa680-labeled polymers was confirmed by visible absorbance at 680 nm. Polyplex micelle solutions prepared at various N/P ratios were ultracentrifuged at 49,000 g for 1 h in order to sediment only the polyplex micelles. The concentration of free polymers contained in the supernatant was calculated using a calibration curve prepared from Alexa680-labeled polymer solutions. The number of block copolymers associating with pDNA was then estimated from the calculated concentration of free polymers.

2.7. Dynamic light scattering (DLS) measurement

The size of the polyplex micelles was evaluated by DLS using Nano ZS (ZEN3600, Malvern Instruments, Ltd., UK). A He–Ne ion laser (633 nm) was used as the incident beam. The concentration of polyplex micelles solutions prepared at various N/P ratios were adjusted to 33.3 μg pDNA/mL in 10 mM Tris–HCl buffer (pH 7.4). Light scattering data was obtained at a detection angle of 173° and a temperature of 37 °C and was subsequently analyzed by the cumulant method to obtain the hydrodynamic diameters and polydispersity indices (PDI) (μ/Γ^2) of the micelles.

2.8. Stability of polyplex micelles against bovine serum albumin (BSA)

Polyplex micelle solution (33.3 μg pDNA/mL) prepared at N/P ratio = 2 was adjusted to 10 μg pDNA/mL in 10 mM Tris–HCl buffer (pH 7.4) with 150 mM NaCl and 0.1 mg/mL BSA. DLS measurements of the polyplex micelle solution were then carried out every 30 min at 37 °C using Nano ZS.

2.9. In vitro transfection

Huh-7 and HeLa cells were separately seeded onto 24-well culture plates (10,000 cells/well) and incubated overnight in 500 μL of Dulbecco's Modified Eagle Medium (DMEM) containing 10% fetal bovine serum (FBS). The medium was exchanged and the pDNA micelle solutions (33.3 μg pDNA/mL) prepared at various N/P ratios were applied to each well at the desired concentrations. The amount of micelle solution added was as follows: 30 μL for 2 μg pDNA/mL, 10 μL for 2/3 μg pDNA/mL, or 2.9 μL for 2/9 μg pDNA/mL. For experiments shown in Fig. 1B (open circles), polymer solution was added to cultured Huh-7 cells simultaneously with PEG-PAsp(DET) micelle (N/P = 4), in order to elucidate the effect of free polymer on transfection efficiency. After 24-h incubation, the medium was replaced with 500 μL of fresh medium, followed by 24-h further incubation. Luciferase gene expression was then evaluated based on photoluminescence intensity using the Luciferase assay kit and a Luminometer (Lumat LB9507, Berthold Technologies, Bad Wildbad, Germany). The amount of protein in each well was concomitantly determined using a Micro BCA protein assay kit. One nanogram of luciferase corresponded to 9.1 × 10⁷ RLU in our experiments according to a standard curve calibrated with recombinant luciferase (QuantiLum, Promega).

2.10. Cytotoxicity of polyplex micelles

Huh-7 and HeLa cells were separately seeded onto 96-well culture plates (2500 cells/well) and incubated overnight in 100 μL of DMEM containing 10% FBS. After the medium was replaced with fresh medium, 7.5 μL of polyplex micelle solution (33.3 μg pDNA/mL) prepared at various N/P ratios was applied to each well (0.25 μg pDNA/well). After 24-h incubation, the medium was replaced with 100 μL of fresh medium, followed by 24-h incubation. Cell viability was evaluated using the MTT assay. Briefly, 20 μL of MTT solution (5 mg/mL in PBS) was added to each well,

followed by 3-h incubation at 37 °C. Then, 100 μL of sodium dodecyl sulfate (SDS) solution (20 w/v% in PBS) was added to dissolve the formed formazan. After 15-min incubation at room temperature, the absorbance from each well was measured at 570 nm. Results were expressed as percentage relative to non-treated controls.

2.11. Cellular uptake of polymers and pDNA

Polyplex micelles were prepared with non-labeled polymer and Cy3-labeled pDNA (Fig. 8A), or with Alexa680-labeled polymer and non-labeled pDNA (Fig. 8B) for these experiments. pDNA was labeled with Cy3 using a Label IT Nucleic Acid Labeling Kit (Mirus, Madison, WI) according to the manufacturer's protocol. Huh-7 cells were seeded on 24-well culture plates (10,000 cells/well) and incubated overnight in 500 μL of DMEM containing 10% FBS. The medium was replaced with fresh medium and then 30 μL of polyplex micelle solution (33.3 μg pDNA/mL) was applied to each well. After 24-h incubation, the medium was removed and the cells were washed 3 times with PBS and detached with trypsin. Harvested cells were re-suspended in PBS and analyzed using the flow cytometer (BD LSR II, BD, Franklin Lakes, NJ).

2.12. Confocal laser scanning microscope (CLSM) observation

pDNA was labeled with Cy5 according to manufacturer's protocol using a Label IT Nucleic Acid Labeling Kit. Huh-7 cells (30,000) were seeded on a 35-mm glass base dish (Iwaki, Tokyo, Japan) and incubated overnight in 1.5 mL of DMEM containing 10% FBS. After the medium was exchanged, 90 μL of polyplex micelle solution (33.3 μg pDNA/mL) was applied to each sample. After 24-h incubation, the medium was removed and the cells were washed three times with PBS. The intracellular distribution of the polyplex micelles was observed by CLSM after staining acidic late endosomes/lysosomes with Lyso Tracker Green (Molecular Probes, Eugene, OR), and nuclei with Hoechst 33342 (Dojindo Laboratories, Kumamoto, Japan). CLSM observation was performed using an LSM 510 (Carl Zeiss, Oberlochen, Germany) equipped with a 63× objective (C-Apochromat, Carl Zeiss) at the excitation wavelengths of 488 nm (Ar laser) for Lyso Tracker Green, 633 nm (He–Ne laser) for Cy5, and 710 nm (MaiTai laser, 2 photon excitation; Spectra-Physics, Mountain View, CA) for Hoechst 33342. To evaluate the endosomal escaping behavior of polyplex micelles, the rate of colocalization of Cy5-labeled pDNA with Lyso Tracker Green was quantified [17]. Colocalization was quantified as follows:

Amount of colocalization(%) = Cy5 pixels$_{colocalization}$/Cy5 pixels$_{total}$ × 100

where Cy5 pixels$_{colocalization}$ represents the number of Cy5 pixels colocalizing with Lyso Tracker Green in the cell, and Cy5 pixels$_{total}$ represents the number of all the Cy5 pixels in the cell.

2.13. Fluorescence correlation spectroscopy (FCS) measurement

PEG-PAsp(DET-Alexa680)-Chole free polymer, polyplex micelles composed of PEG-PAsp(DET-Alexa680)-Chole and pDNA, and polyplex micelles composed of PEG-PAsp(DET)-Chole and Cy5-labeled pDNA, were used in this experiment. Block copolymers and polyplex micelles (N/P = 8) were adjusted to a polymer concentration of 187 μg/mL (33.3 μg pDNA/mL), and then diluted to a concentration of 18.7 μg/mL using 10 mM Hepes buffer (pH 7.3) (Fig. 10A) or 10 mM MES buffer (pH 5.5) (Fig. 10B), or 2.08 μg/mL using 10 mM Hepes buffer (pH 7.3) (Fig. 10A). FCS measurements were carried out using an LSM 510 (Carl Zeiss) equipped with a 40× objective (C-Apochromat, Carl Zeiss) and the ConfoCor3 module. Excitation of Alexa680 and Cy5 was achieved with a He–Ne laser (633 nm). The relative diffusion times of polymer and micelles (Fig. 10A) were determined using PEG-PAsp(DET-Alexa680)-Chole solution and its polyplex micelle solution, respectively. Furthermore, the percentage of polymers associating with pDNA in the micelle solution was calculated as follows:

Percentage of polymers associating with pDNA =

$$\left[\frac{Nfp\,_{PEG-PAsp(DET-Alexa680)-Chole} - \left(Nfp\,_{PEG-PAsp(DET)-Chole/pDNA} - Nfp\,_{PEG-PAsp(DET)-Chole/Cy5-pDNA} \right)}{Nfp\,_{PEG-PAsp(DET-Alexa680)-Chole}} \right] \times 100$$

where Nfp $_{PEG-PAsp(DET-Alexa680)-Chole}$ represents the number of fluorescent particles (free polymers) in PEG-PAsp(DET-Alexa680)-Chole solution, Nfp $_{PEG-PAsp(DET-Alexa680)-Chole/pDNA}$ represents the number of fluorescent species (free polymers and micelles) in PEG-PAsp(DET-Alexa680)/pDNA micelle solution, and Nfp $_{PEG-PAsp(DET)-Chole/Cy5-pDNA}$ represents the number of fluorescent species (micelles) in PEG-PAsp (DET)-Chole/Cy5-pDNA micelle solution.

2.14. Stability of polyplex micelles in the blood stream

Polyplex micelles (N/P = 8) incorporating Cy5-labeled pDNA (100 μg pDNA/mL, 200 μL) in 10 mM Hepes buffer (pH 7.3) with 150 mM NaCl were intravenously injected into the tail vein of balb/c mice at a dose of 20 μg pDNA/mouse. Blood

Scheme 1. Synthesis of PEG-PAsp(DET)-Chole block copolymer.
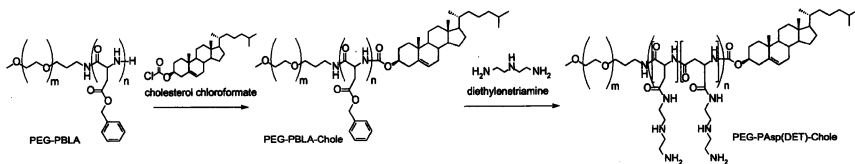
was collected from the postcaval vein under anesthesia at appointed times after injection, followed by centrifugation to obtain the plasma. Two microliters of 10× trypsin-EDTA were added to 20 μL of the obtained plasma and incubated at 37 °C overnight. The fluorescence intensity of the sample solution was measured using a spectrofluorometer (ND-3300, NanoDrop). The injected dose (%) was calculated using a standard curve.

2.15. Anti-tumor activity assay

Balb/c nude mice were inoculated subcutaneously with human pancreatic adenocarcinoma BxPC3 cells (5 × 10⁶ cells in 100 μL of PBS). Tumors were allowed to grow for 2–3 weeks to reach proliferative phase (approximately 45 mm³). Subsequently, polyplex micelles loading pDNA encoding sFlt-1 (20 μg pDNA/mouse) in 10 mM Hepes buffer (pH 7.3) with 150 mM NaCl were injected into the tail vein 3 times at 4-day intervals. Tumor volume (V) was calculated as the following equation:

$$V = a \times b^2/2$$

where a and b denote the long and short diameters of the tumor tissue, respectively.

3. Results

3.1. Ultracentrifugation analysis of PEG-PAsp(DET) polyplex micelles

The amount of free block copolymer in PEG-PAsp(DET) micelle solutions was quantified by ultracentrifugation analysis of polyplex micelles prepared with fluorescent-labeled block copolymer [PEG-PAsp(DET-Alexa680)]. Polyplex micelles were confirmed to precipitate after 1 h of ultracentrifugation at 49,000 g, whereas free block copolymers could not sediment (data not shown). Thus, the amount of free block copolymers was estimated by visible absorbance at 680 nm. Fig. 1A shows the number of block copolymers associating with a pDNA in the polyplex micelle solution prepared at each N/P ratio. Note that a stoichiometric charge ratio of PEG-
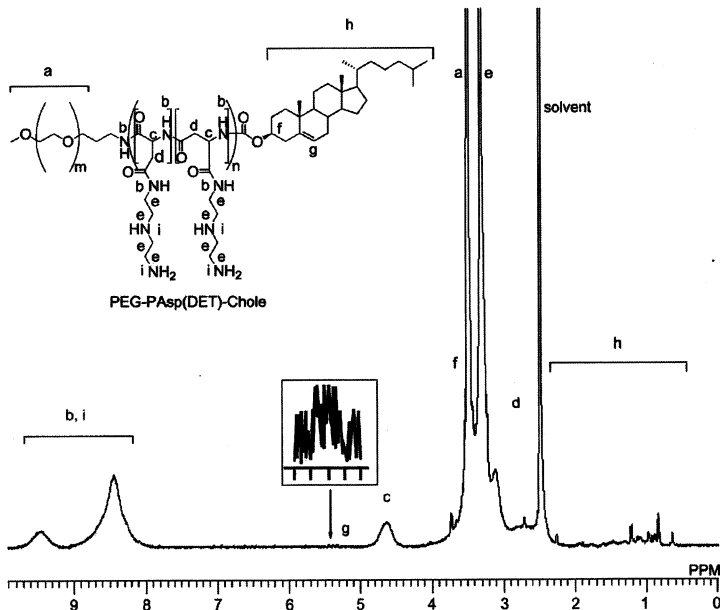

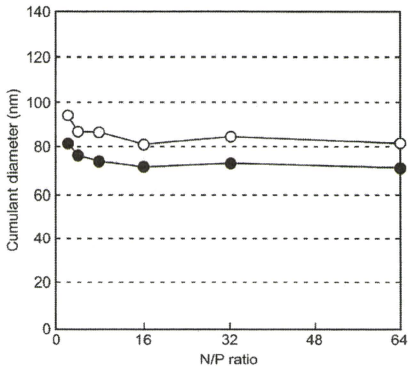**Fig. 2.** ¹H NMR spectrum of PEG-PAsp(DET)-Chole block copolymer in DMSO at 25 °C.

Fig. 3. Cumulant diameters of PEG-PAsp(DET) (closed circles) and PEG-PAsp(DET)-Chole (open circles) polyplex micelles,

PAsp(DET) micelle should be $N/P = 2$ ($N^+/P = 1$) because half of the amino groups in PAsp(DET) are protonated at pH 7.4 [11]. The number of block copolymers associating with a pDNA at $N/P = 2$ and at $N/P \geq 4$ ($N^+/P \geq 2$) was estimated to be 150 and approximately 190, respectively by the results obtained by ultracentrifugation experiments. The theoretical number of block copolymers associating with a pDNA at stoichiometric charge ratio was calculated to be 189 based on complete neutralization of PAsp(DET) with a polymerization degree = 68 and pDNA with 6411 bp long. This result indicated that PEG-PAsp(DET)/pDNA polyplex micelles at $N/P \geq 4$ ($N^+/P \geq 2$) were formed at polymer/pDNA charge ratio = 1/1 (polymer/pDNA molar ratio = 190/1), and that the block copolymers present in solution in excess of that ratio should exist as free polymers at this concentration.
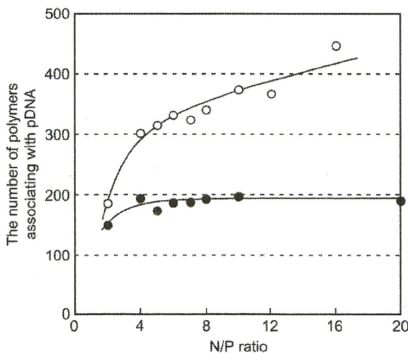

Fig. 4. The number of PEG-PAsp(DET-Alexa680) (closed circles) and PEG-PAsp(DET-Alexa680)-Chole (open circles) block copolymers associating with a pDNA.
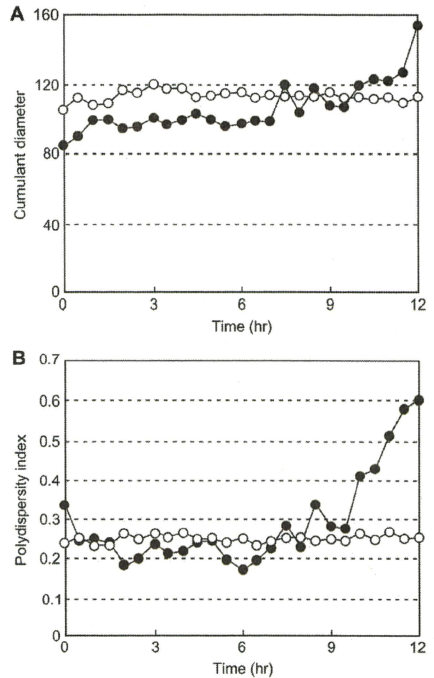
Fig. 5. Time-dependent change of cumulant diameters (A) and polydispersity index (PDI: μ/Γ^2) (B) of polyplex micelles ($N/P = 2$) in the presence of bovine serum albumin (0.1 mg/mL). Closed circles: PEG-PAsp(DET) polyplex micelles. Open circles: PEG-PAsp(DET)-Chole polyplex micelles.

3.2. In vitro transfection efficiency of PEG-PAsp(DET) polyplex micelles

In order to confirm the effects of free polymer on in vitro transfection, we evaluated the transfection efficiency of PEG-PAsp(DET) micelles in Huh-7 cells under the following conditions: (i) polyplex micelles prepared at each N/P ratio; (ii) polyplex micelles prepared with PEG-PAsp(DET) at $N/P = 4$ with addition of free polymer to achieve the same polymer concentration achieved at each N/P ratio used in condition (i). Under the conventional transfection conditions used in (i) above, the transfection efficiency increased with N/P ratio as previously reported [11]. Surprisingly, the profile of transfection efficiency under the condition (ii) showed the same behavior as that under the condition (i) with the addition of free polymer as shown in Fig. 1B. These results imply that increased transfection efficiency of PEG-PAsp(DET) micelles prepared at high N/P ratios might involve the effect of non-associating polymers with pDNA in the culture medium.

3.3. Synthesis of PEG-PAsp(DET)-Chole block copolymer

PEG-PAsp(DET)-Chole was synthesized using PEG-PBLA (PEG: 12,000 g/mol, polymerization degree of PBLA segment: 68) [11] as a starting material (Scheme 1). Addition of excessive cholesterol chloroformate and TEA to PEG-PBLA, which possessed a primary amino group in the terminus of PBLA, afforded PEG-PBLA-Chole with ω-terminus of cholesterol. Conversion of PBLA segment into PAsp(DET) segment was achieved by aminolysis reaction [18]. Introduction rates of cholesterol and ethanediamine were determined by ^{1}H NMR analysis (Fig. 2) based on the peak intensity ratio of the methylene protons of PEG (OCH$_2$CH$_2$, δ = 3.6 ppm) to the vinyl proton of cholesterol (C=CHCH$_2$, δ = 5.4 ppm), or to the methylene protons of DET (NHCH$_2$CH$_2$NHCH$_2$CH$_2$NH$_2$, δ = 3.1–3.5 ppm), respectively. Cholesterol introduction and the aminolysis reaction were confirmed to proceed quantitatively.

3.4. Formation of PEG-PAsp(DET)-Chole polyplex micelles

Agarose gel electrophoresis showed that free pDNA was not detected in both PEG-PAsp(DET) and PEG-PAsp(DET)-Chole micelles at N/P > 1.75 (N$^+$/P > 0.875) (data not shown), confirming that all of the pDNA were entrapped in polyplex micelles. Complex formation of pDNA with PEG-PAsp(DET) at pH 7.4 was previously reported to reach completion at N/P ≈ 2 (N$^+$/P ≈ 1) [11,19], which is consistent with the result obtained in this work. Complex formation was not hindered by cholesterol introduction into the

PAsp(DET) segment of the block copolymer as the N$^+$/P for complete pDNA entrapment did not change compared to the parent polymer. The size of the polyplex micelles was evaluated by DLS (Fig. 3). The cumulant diameters of polyplex micelles prepared with both block copolymers were found to be approximately 70–80 nm by DLS measurement.

3.5. Ultracentrifugation analysis of PEG-PAsp(DET)-Chole polyplex micelles

The amount of free polymer in PEG-PAsp(DET)-Chole micelle solution was also quantified by the same method as described for micelles prepared with PEG-PAsp(DET). As shown in Fig. 4, the number of polymers associating with a pDNA at N/P = 2 (N$^+$/P = 1) was approximately 190, which corresponds to the stoichiometric value. However, at N/P > 2 (N$^+$/P > 1), micelles formed with PEG-PAsp(DET)-Chole exhibited an increased number of polymers in the polyplex (in excess of the stoichiometric charge ratio), whereas micelles prepared with PEG-PAsp(DET) showed a constant number of associated polymers.

3.6. Stability of polyplex micelles against bovine serum albumin (BSA)

PEG-PAsp(DET) micelles have high transfection ability with low cytotoxicity at high N/P ratios, however, they are unstable and easily decondensed in the medium containing serum [20], probably
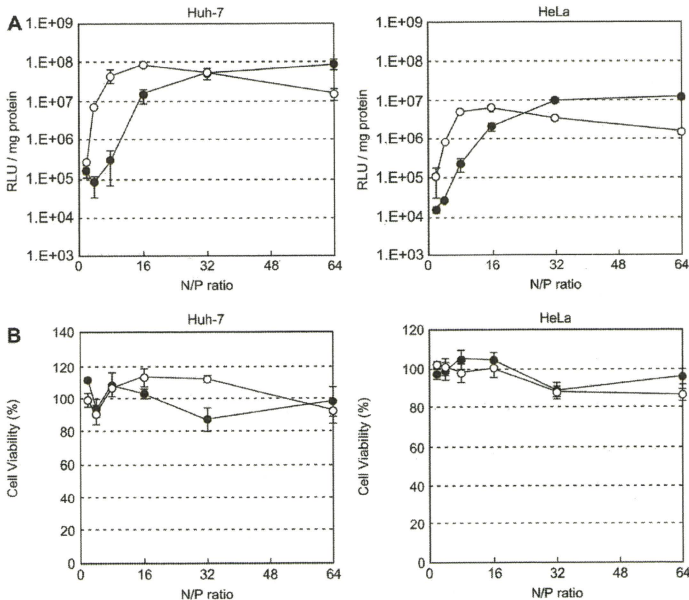

Fig. 6. Transfection efficiency (A) and cytotoxicity (B) of polyplex micelles prepared at various N/P ratios against Huh-7 cells and HeLa cells. Closed circles: PEG-PAsp(DET) polyplex micelles. Open circles: PEG-PAsp(DET)-Chole polyplex micelles. Error bars in the graph represent SEM, n = 4.

due to the weak association power of PAsp(DET) segment with pDNA. Therefore, the stability of polyplex micelles containing cholesterol was compared to micelles without cholesterol by monitoring the time-dependent change of cumulant diameter and PDI in the presence of BSA (Fig. 5). After adding BSA (0.1 mg/mL) to polyplex micelle solution (prepared at N/P = 2), the cumulant diameter and PDI were measured every 30 min. PEG-PAsp(DET)-Chole micelles maintained their initial size and PDI for 12 h (Fig. 5A). On the other hand, the size and PDI of micelles prepared with PEG-PAsp(DET) remained constant for only ~6 h and then gradually increased, and monodispersity was not maintained (Fig. 5B). These results imply that cholesterol introduction resulted in increased stability of polyplex micelles in BSA solution.

3.7. In vitro transfection efficiency and cytotoxicity of polyplex micelles

The in vitro transfection efficiency of PEG-PAsp(DET) and PEG-PAsp(DET)-Chole micelles prepared at various N/P ratios was evaluated against Huh-7 and HeLa cells by the luciferase assay (Fig. 6A). Transfection efficiencies of PEG-PAsp(DET) micelles increased with N/P ratio, and reached a maximum at N/P 32–64. However, PEG-PAsp(DET)-Chole micelles showed the highest transfection efficiencies at N/P = 8–16, with maximum transfection levels comparable to PEG-PAsp(DET). Cholesterol introduction clearly enhanced transfection efficiency at lower N/P ratios, especially at N/P 4 and 8. Fig. 6B shows the results of cytotoxicity analysis performed under the same condition as the luciferase assay. Increased cytotoxicity as a result of cholesteryl introduction was not detected in Huh-7 and HeLa cells.

3.8. Effect of pDNA concentration on transfection efficiency

All transfection experiments in the preceding section were carried out at a constant pDNA concentration of 2 μg pDNA/mL (1 μg pDNA/well, 24-well plate) (Fig. 6). Here additional transfection experiments were repeated against Huh-7 cells at the diluted concentration of 2, 2/3, and 2/9 μg pDNA/mL in order to confirm the influence of dilution (Fig. 7). The transfection efficiency of PEG-PAsp(DET) micelles markedly decreased with reduced pDNA concentration (Fig. 7A), while of the transfection ability of PEG-PAsp(DET)-Chole micelles was maintained without a severe decrease (Fig. 7B). PEG-PAsp(DET) micelles at N/P = 16 showed approximately 1/1000 of transfection efficiency in response to the concentration change from 2 μg to 2/9 μg pDNA/mL. In contrast, the decrease in the transfection with PEG-PAsp(DET)-Chole micelles was less than 1/10. Thus, transfection efficiency of PEG-PAsp(DET)-Chole micelles was confirmed to be more tolerable in dilution compared to PEG-PAsp(DET) micelles, suggesting their feasibility for in vivo gene delivery, which requires high transfection ability under highly diluted conditions.

3.9. Cellular uptake of micelles

Flow cytometric analysis was used to quantify the cellular uptake of micelles with respect to pDNA (Fig. 8A) and polymer (Fig. 8B) by using Cy3-labeled pDNA and Alexa680-labeled polymer, respectively. PEG-PAsp(DET)-Chole micelles showed higher pDNA uptake than PEG-PAsp(DET) micelles at both N/P = 8 and 16 (Fig. 8A). Cholesterol introduction enhanced the stability of polyplex micelles against BSA (shown in Fig. 5), thus, PEG-PAsp (DET)-Chole micelles likely maintained their structures without dissociation or aggregation in the cell culture medium, which likely increased the uptake of pDNA. The cellular uptake of polymer was

also higher for PEG-PAsp(DET)-Chole than PEG-PAsp(DET) (Fig. 8B). PEG-PAsp(DET)-Chole polymers might be more effectively internalized into the cells due to their strong association power towards pDNA.

3.10. CLSM observation and evaluation of endosomal escape

The intracellular distribution of polyplex micelles was investigated by CLSM using Cy5-labeled pDNA (red) incorporated micelles (Fig. 9A). Lyso Tracker Green (green) and Hoechst 33342 (blue) were used to label late endosomes/lysosomes and nuclei, respectively. The amount of Cy5-pDNA observed in the cells was much higher for PEG-PAsp(DET)-Chole micelles than PEG-PAsp (DET) micelles at both N/P = 8 and 16, which was consistent with the results obtained by flow cytometric analysis (Fig. 8A). Colocalization of pDNA with the late endosomes/lysosomes was
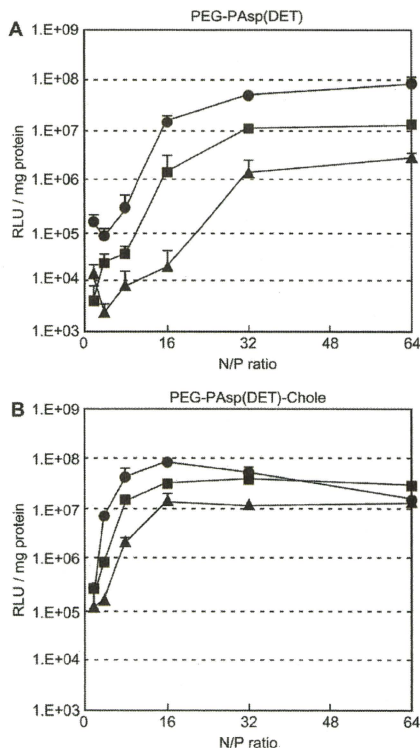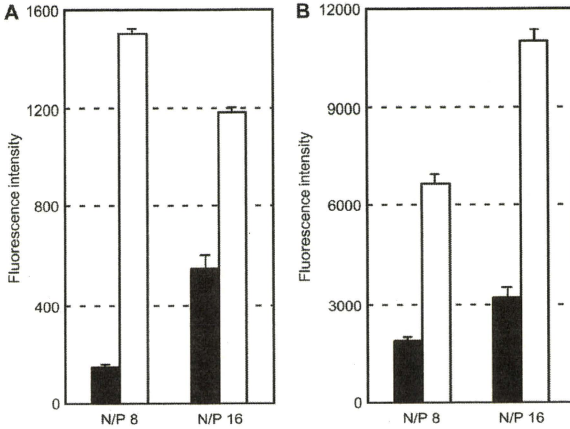
Fig. 7. Effect of pDNA concentration on transfection efficiency of PEG-PAsp(DET) (A) and PEG-PAsp(DET)-Chole (B) polyplex micelles against Huh-7 cells. Closed circles, squares, and triangles represent 2 μg/mL, 2/3 μg/mL, and 2/9 μg/mL of pDNA concentration in the culture medium, respectively. Error bars in the graph represent SEM, n = 4.
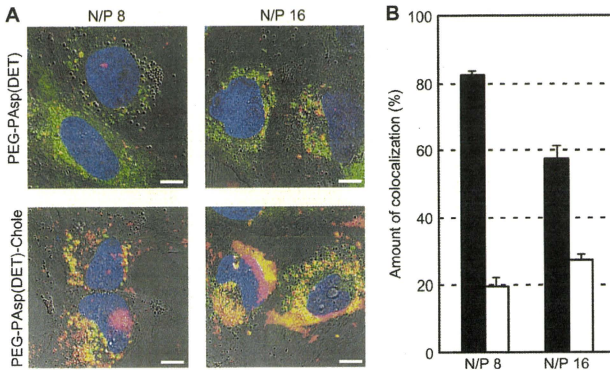
Fig. 8. Cellular uptake of Cy3-labeled pDNA (A) and Alexa680-labeled polymers (B). Closed bars: PEG-PAsp(DET) polyplex micelles. Open bars: PEG-PAsp(DET)-Chole polyplex micelles. Error bars in the graph represent SEM, $n = 4$.

quantified and shown in Fig. 9B. At N/P = 8, more than 80% of pDNA in PEG-PAsp(DET) micelles was localized in the late endosomes/lysosomes, while only 20% of that in PEG-PAsp(DET)-Chole micelles was localized there. These results revealed that PEG-PAsp(DET)-Chole micelles internalized into the cells could achieve effective endosomal escape. Note that increasing N/P ratio appreciably decreased the endosomal/lysosomal entrapment of PEG-PAsp(DET) micelles from more than 80% to less than 60%, consistent with the result of the transfection efficiency (Fig. 6).

3.11. FCS measurement

FCS analysis was performed in order to estimate a change in the association state of polyplex micelles with respect to dilution and pH (Fig. 10). At pH 7.3, the relative diffusion time of PEG-PAsp (DET)-Chole micelle solution was approximately 8-fold higher than that of PEG-PAsp(DET)-Chole polymer solution, and the diffusion time was not significantly changed by 9-fold dilution (Fig. 10A). These results suggest that the association state of PEG-PAsp(DET)-Chole micelles remains constant in this concentration range, which

Fig. 9. (A) CLSM observation of the intracellular distribution of polyplex micelles containing Cy5-labeled pDNA (red) with late endosomes/lysosomes (green) and nuclei (blue) stained using Lyso Tracker Green and Hoechst 33342, respectively. Bars represent 10 μm. (B) Quantification of Cy5-labeled pDNA colocalization with Lyso Tracker Green in the Huh-7 cells. Closed bars: PEG-PAsp(DET) polyplex micelles. Open bars: PEG-PAsp(DET)-Chole polyplex micelles. Error bars in the graph represent SEM, $n = 10$.